Optics Letters

# Pseudo-gray-scale halftone gratings for shearing and Hartmann wavefront sensors

Kenneth A. Goldberg

*Advanced Light Source, Lawrence Berkeley National Laboratory, 1 Cyclotron Road, Berkeley, California 94720, USA (kagoldberg@lbl.gov)*

*Received 11 December 2020; revised 7 January 2021; accepted 8 January 2021; posted 8 January 2021 (Doc. ID 417408); published 3 February 2021*

**Now in use on x-ray beamlines worldwide, shearing interferometry and Hartmann wavefront sensing provide effective feedback for measuring and optimizing high-quality beams. Conventionally, both approaches spatially modulate the beam properties (amplitude or phase) using two-tone, binary patterns, leading to deleterious diffraction effects that must be mitigated. In shearing, the presence of multiple diffraction orders affects measurement near boundaries. In Hartmann, diffraction limits the measurement point density. We demonstrate that the use of pseudo-gray-scale halftone patterns in the diffracting elements can improve the performance of both techniques.** 

https://doi.org/10.1364/OL.417408

In recent years, shearing interferometry and Hartmann testing have emerged as effective and easily implemented wavefront sensing techniques for short-wavelength applications. Complementing the creation of high-coherent-flux light sources, advanced beamline optical systems for soft x ray, tender x ray, and hard x ray photon energies are reaching toward and achieving diffraction-limited optical performance. This capability comes largely from improvements in mirror fabrication and from the advent of adaptive optical elements coupled to feedback from wavefront sensors.

Shearing is an interferometric approach that uses a diffraction grating to produce displaced copies of the test wavefront that overlap at the detection plane [1–4]. The most common configurations are designed to exploit the Talbot self-imaging condition, reproducing a high-contrast pattern while revealing aberrations in the input wavefront.

In the Hartmann test, a grid of holes in an opaque screen projects isolated, non-interfering beamlets onto the detection plane [5–8]. Measured displacements show the local wavefront slope across the beam. While shearing can use amplitude-modulating or phase-shifting gratings, Hartmann requires high contrast (i.e., opacity) to achieve a high signal-to-noise ratio. The two techniques are shown schematically in Fig. 1.

To my knowledge, all reported x ray applications of these techniques have used binary (i.e., two-tone) amplitude or phase elements, patterned for shearing as square-wave line patterns [4,9], cross-gratings [1], or checkerboards [10], and for Hartmann as open round or square holes [8] in an opaque screen (see Fig. 2).

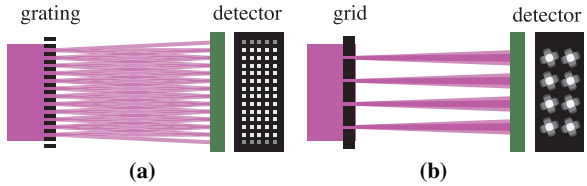


**Fig. 1.** Schematic representations of (a) single-grating shearing interferometry and (b) Hartmann wavefront sensing, two complementary approaches to wavefront measurement. The beam is incident from the left.

X ray transmission gratings are created with various lithographic patterning techniques. Feature sizes are on the micron to tens-of-microns scale for extreme ultraviolet, soft x ray and hard x ray shearing, and Hartmann applications.

In many forms of interferometric measurement, mutually coherent test and reference beams interfere, and the resultant fringes reveal path length differences. Shearing, however, compares a test beam with displaced copies of itself. In *single-grating* shearing configurations, the presence of multiple displaced beams, emanating with various amplitudes from the grating's diffraction orders, complicates the reconstruction near pupil boundaries and small features (see Fig. 3).

One implementation uses an image-plane spatial filter to block all but two beams in each direction [2]. The Ronchi configuration shifts the beams by half the beam width [11], creating two-beam interference. However, most *single-grating* applications use a small shear magnitude to achieve a near total overlap of the shifted beams across the aperture.

In the Hartmann case, diffraction causes the beamlets to spread outward toward their neighbors, degrading measurement or forcing the use of a grid with a larger hole-spacing. Rotating the orientation of square holes [Fig. 2(f)] mitigates this overlap to some extent by steering diffracted light between neighboring beamlets [6].

Here, I propose the use of pseudo-gray-scale, halftone patterns to approximate smooth screen-transmission functions and reduce the deleterious effects of diffraction. We can reduce the amplitude of the higher-ordered beams in shearing and narrow the diffraction-spread of Hartmann beamlets (i.e., sidelobe suppression) by pattern modulation at finer length scales. This leaves the fundamental design of the elements intact while improving their relative performance. With micron-scale

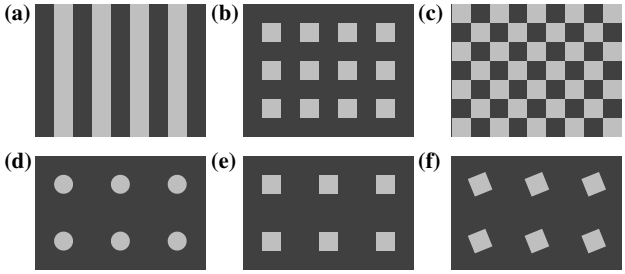


**Fig. 2.** Details of common grating types used for shearing wavefront sensors: (a) linear grating, (b) cross-grating, and (c) checkerboard. The two tones can modulate amplitude (e.g., opaque and transparent), phase, or both. Hartmann grids: (d) circular holes, (e) square holes, and (f) rotated square holes.

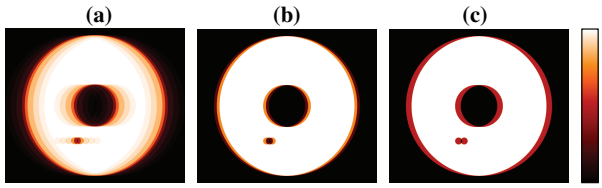


**Fig. 3.** Multi-beam overlap in 1D shearing is illustrated for an annular pupil with a dark defect and three different grating types, as labeled. The pupil amplitudes shown here sum up to 15 weighted and shifted diffraction orders. Boundaries and sharp features compromise wavefront analysis locally. (a) Square-wave amplitude. (b) Sinusoidal amplitude. (c) Sinusoidal $\pi$-phase.

patterns, sub-micron patterning is well within reach. Halftones have been used in the fabrication of kinoform diffractive optical elements [12] and photomask patterns for similar purposes [13]. The benefits of this approach are apparent through spatial and spatial-frequency descriptions of the devices.

The shearing grating patterns may be described using periodic, piecewise-continuous, two-level transmission functions, with complex values $a$ and $b$, and a spatial period, or *pitch*, $L$. For the conventional patterns, we use a rectangle or boxcar function, assigning 1 to $a$ and 0 to $b$, and we set an equal period in both $x$ and $y$ directions. We define a function $\Pi(t)$ over a single period, with a *duty-cycle* parameter $d \in [0,\ 1]$ for the linear ratio, such that with $t \in [0,\ L]$,

$$\Pi(t) = \begin{cases} 1, & 0 \le t < dL \\ 0, & dL \le t < L \end{cases}. \tag{1}$$

Commonly, $d = 0.5$. The shearing gratings in Fig. 2 can be described as (a) $\Pi(x)$, (b) $\Pi(x)\Pi(y)$, and (c) $\Pi(x) \oplus \Pi(y)$, where the $\oplus$ symbol represents the XOR operation.

From a spatially uniform incident wave, the variation in the transmitted field, $U_0(\mathbf{r})$, comes only from the screen. With pattern features much larger than the wavelengths of interest, and detector distances much greater than the lateral widths under consideration, the diffraction-order amplitudes are well described by the Fourier transformation of the field at the screen, $\mathcal{F}\{U_0(\mathbf{r})\}$. For periodic structures illuminated by a coherent monochromatic beam, the angular-spectrum reveals the amplitudes of the various diffracted orders. Partially coherent and spectrally broad extensions can be made from this basic case.

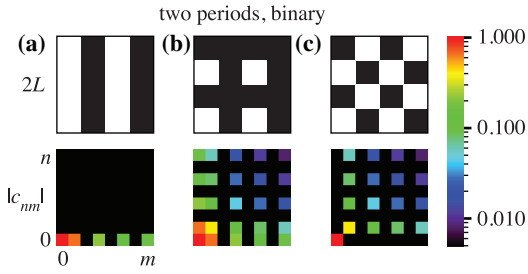


**Fig. 4.** Grating patterns and Fourier spectra for the three conventional grating types in Figs. 2(a)–2(c). Shown are $2 \times 2$-period details of the grating patterns $c(x, y)$, with $d = 0.5$, alongside the first $8 \times 8$ Fourier coefficients, $c_{m,n}$, calculated from Eq. (3). Within each case, the absolute values of the coefficients are normalized to $c_{0,0}$ (lower-left, red square). Central portions of the first quadrant are shown. Colors represent a logarithmic scale.

With $k = 2\pi/L$, the patterns $c(x, y)$ can be decomposed into complex, double Fourier series, and the Fourier coefficients can be solved with Dirchelet (periodic) boundary conditions,

$$c(x, y) = \sum_{m,n=-\infty}^{\infty} c_{m,n} e^{ikmx} e^{ikny}, \tag{2}$$

$$c_{m,n} = \frac{1}{L^2} \int_0^L \int_0^L c(x, y) e^{-ikmx} e^{-ikny}\, \mathrm{d}x\mathrm{d}y. \tag{3}$$

These coefficients describe the complex amplitudes of the interfering beams. When only two beams are present for each orthogonal shear direction, the only non-zero values are the paired coefficients $\{c_{-1,0},\ c_{1,0}\}$ for $x$, and $\{c_{0,-1},\ c_{0,1}\}$ for $y$. Multi-beam interference in the unfiltered, single-grating shearing implementations can be characterized by the series of coefficient amplitudes. The Fourier spectra of conventional gratings shown in Fig. 4 reveal the presence of many orders.

Shearing interferograms are commonly analyzed using the Fourier transform method of fringe pattern analysis, filtering the spatial-frequency domain to select the interferences among specific orders [1,14]. However by operating on the intensity pattern, the filtering nonetheless allows the interaction of other, different order pairs to affect the resultant measurement. For example, in the Fourier transform of the measured intensity, the interaction of the $-1$st- and 1st-order beams occupies the same spatial frequency as the interaction of the 3rd- and 5th-order beams. Similarly, contributions from the interactions of all pairs of beams for which the index difference is 1 overlap in the first frequency. Since interferograms are real valued, the Fourier coefficients form polar-symmetric, equal-valued pairs: $c_{m,n} = c_{-m,-n}$.

Limiting the number of interfering beams can improve single-grating shearing interferometry, and we can shape the Fourier spectrum to achieve that. In this way, we can view conventional square-wave gratings as coarse approximations to optimized cases. It is theoretically possible to create two- or three-beam interferences from a single grating using sinusoidal transmission functions in amplitude or phase. Modulation of the form $f(x) = \frac{1}{2}[1 + \sin(2\pi x/L)]$ generates only 0th-order and $\pm 1$st-order Fourier coefficients. Sinusoidal amplitude modulations are shown in Fig. 5. (Note that $\pi$-phase modulation is a special case where it is possible to extinguish the 0th order [10].)

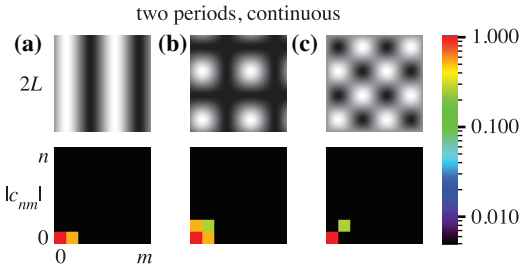


**Fig. 5.** Continuous-tone versions of the gratings of Fig. 4 with sinusoidal amplitude transmission functions. The coefficient amplitudes show that only the 0th-order and 1st-order beams would be present in the interferograms.

Recognizing that the grating lines and Hartmann grid holes used at x ray wavelengths are typically much larger than the patterning resolution of available lithography techniques, we can use halftone patterns to approximate the optimal transmission functions. Commonly seen in newspaper and magazine image rendering, halftoning is a class of techniques that uses two brightness levels and fine patterning to approximate continuously varying intensities, forming a pseudo-gray scale.

There are a number of mathematical approaches to halftoning [15]. Simple methods spatially modulate the density of uniformly sized points or the sizes of regularly spaced points to control the open-area fraction across the screen. Selection and optimization of the halftone mode depends on the characteristics of the lithography and the pattern dimensions and is beyond the scope of this article.

Figure 6 shows examples of halftoned approximations to the shearing gratings from Fig. 5, rendered with two different halftone resolutions: 90 and 60 pixels per period. The halftones were calculated in the following way. Ideal sinusoidal field-amplitude patterns were rendered on a grid, downsampled to 30 or 20 samples per period and reduced to 10 gray scale levels, 0 through 9. Each point was then replaced with a 3 × 3-pixel, binary grid, randomly generated with the number of bright pixels matching the gray scale level. Another approach is to treat the normalized, downsampled ideal pattern as a probability distribution and compare it, point-by-point, to uniformly distributed random values between 0 and 1.

The halftones' Fourier spectra show us that higher-orders are present with significantly reduced amplitudes relative to the conventional gratings in Fig. 4. The higher halftone pixel density case comes closer to the ideal values from Fig. 5.

Challenges in Hartmann testing can also be addressed with halftone patterns. Diffraction is an important aspect that governs the sensitivity of Hartmann wavefront slope measurements. Optimal grids would produce compact beamlets that do not overlap neighboring measurement points. Square and circular grid holes produce well-known sinc and Airy diffraction patterns with lobes and rings that extend outward from the center. A Gaussian transmission pattern would produce the kind of spot we seek, so we evaluate halftone approximations to it. We note that diffraction from non-Gaussian, apodized aperture shapes has been investigated in many contexts, including sidelobe suppression and beam divergence control [16].

Figure 7 shows diffraction patterns from six ideal and halftoned apertures. Coherent-wave Fresnel diffraction calculations [17] are made for 1 nm wavelength and 200 mm distance from the aperture to the detector plane. The circular aperture

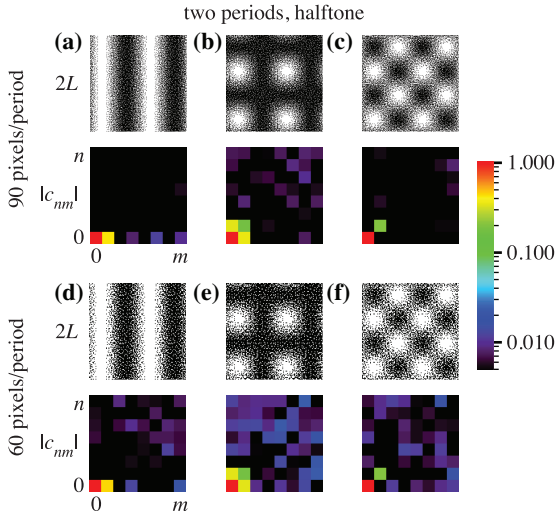


**Fig. 6.** Halftone versions of the optimal gratings of Fig. 5 and their Fourier spectra. The patterns in (a), (b), and (c) were halftoned to 90 pixels per period. The patterns in (d), (e), and (f) were halftoned to 60 pixels per period.

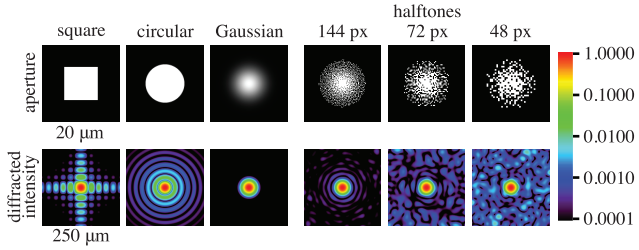


**Fig. 7.** Ideal and halftoned Hartmann apertures and their diffraction patterns, computed for $\lambda = 1$ nm and $z = 200$ mm. The ideal apertures are square, $w = 8.70$ μm; circular, $d = 10$ μm; and Gaussian amplitude, $\exp[-(r/a)^2]$ with $a = 7.26$ μm. The three halftones approximate the Gaussian aperture with 144, 72, and 48 pixels per 10 μm, respectively. The diffracted intensities are shown on a logarithmic color scale.

has 10 μm diameter, and the sizes of the square and Gaussian transmission apertures are selected to approximately match the same full width at half-maximum (FWHM) value. This is approximately 8.70 μm width for the square, and $\exp[-(r/a)^2]$ with $a = 7.26$ μm for the Gaussian.

Three halftone approximations of the Gaussian transmission are shown with varying pixel densities of 144, 72, and 48 pixels per 10 μm width, respectively. Relative to the smoothly attenuating Gaussian pattern, the lobes and rings of the square and circular apertures have significant intensity in the region from 15 to 40 μm radius. The halftone cases approach the Gaussian intensity profile with a low-intensity speckle pattern that decreases with increasing halftone pixel density.

The halftone approach can work for one-dimensional shearing and Hartmann testing as well, where holes are replaced with lines and the wavefront slope is measured in only one direction. Such grids are being planned as feedback for adaptive x ray optics (i.e., bendable mirrors) [4,18]. Figure 8 shows line patterns and their diffracted intensities. Included are a conventional 10 μm line; Gaussian amplitude, $\exp[-(x/a)^2]$ with $a = 4.41$ μm (selected to have the same diffracted FWHM); and linear

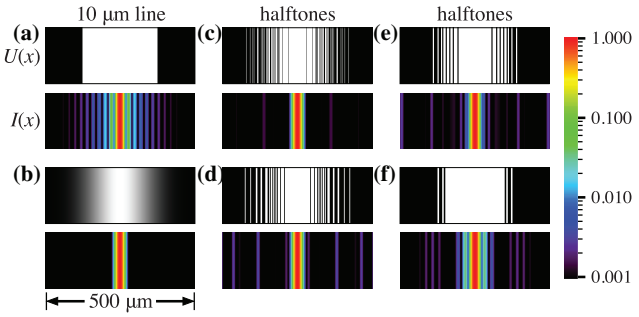


**Fig. 8.** Details of 1D, ideal vertical Hartmann grid lines, and halftone versions, shown with their intensity patterns. (a) A 10 μm line. (b) Gaussian. Halftone lines with (c) 192, (d) 48, (e) 32, and (f) 24 pixels per 10 μm.

halftone approximations of the Gaussian case with varying pixel density. As before, $\lambda = 1$ nm, and $z = 200$ mm.

One-dimensional halftone patterns were randomly generated using the Gaussian amplitude as a probability for each pixel to be open. Mirror-symmetry was imposed to prevent lateral position variation in the diffraction pattern. Separately, for each of the four pixel densities, the halftones shown in Fig. 8 were selected from 5,000 randomly generated cases, minimizing a distance-weighted-intensity merit function. The halftone diffraction patterns show significant sidelobe suppression relative to the conventional line, improving with increased pixel density.

Beyond Gaussian amplitude transmission, it is worth considering the benefit of a Shack–Hartmann approach in transmission, turning the lines and holes into focusing diffractive lenslets, photon sieves [19], or hole arrays [20], including halftoned versions, especially for cases where the energy bandwidth is limited. Arrays of reflective zone plates for this purpose have been demonstrated at 46.9 nm wavelength [21].

In sum, for shearing interferometry and Hartmann wavefront sensing, the pseudo-gray-scale halftone approach can optimize the properties of the diffracted beams and improve the resultant wavefront measurements. This is especially true when the screen fabrication supports the creation of arbitrary, pixelated patterns with sufficient density. Performance improves with higher pixel densities, up to the point where transmission is reduced by small feature sizes. That is, while the diffraction properties would be largely insensitive to the shape of individual pixels, they should be sufficiently large that transmission is predictable.

Data analysis in both shearing and Hartmann testing measures small, relative displacements in the spot or line patterns. Therefore, to avoid undesirable variation from feature to feature, the same calculated halftone pattern can be applied in a repeating manner at each feature. In this way, the irregularities from the halftoning simply repeat periodically and do not induce spot-to-spot or line-to-line offsets. Otherwise, the inherent variations would have to be treated as systematic errors and removed in calibration.

Much as the Hartmann strategy of rotated squares helps to avoid overlap among neighboring beams, there may be additional ways to engineer the halftone patterns to knock out certain spatial frequencies or angle ranges in the diffracted light, protecting adjacent beams from overlap.

The shearing and Hartmann methods are sensitive to spectral bandwidth and spatial coherence, and such considerations must be included when developing case-specific designs. I anticipate that the inclusion of pseudo-gray-scale halftones will not significantly change those sensitivities except to reduce speckle contrast in the presence of partial coherence or finite bandwidth.

**Funding.** Director, Office of Science, Office of Basic Energy Sciences of the U.S. Department of Energy (DE-AC02-05CH11231).

**Acknowledgment.** Antoine Wojdyla provided helpful feedback on this work. I am grateful for the support of Howard Padmore and Elaine DiMasi.

**Disclosures.** The author declares no conflicts of interest.

## REFERENCES

1. P. P. Naulleau, K. A. Goldberg, and J. Bokor, J. Vac. Sci. Technol. B **18**, 2939 (2000).
2. K. Sugisaki, M. Okada, K. Otaki, Y. Zhu, J. Kawakami, K. Murakami, C. Ouchi, M. Hasegawa, S. Kato, T. Hasegawa, H. Yokota, T. Honda, and M. Niibe, Proc. SPIE **6921**, 788 (2008).
3. S. Matsuyama, H. Yokoyama, R. Fukui, Y. Kohmura, K. Tamasaku, M. Yabashi, W. Yashiro, A. Momose, T. Ishikawa, and K. Yamauchi, Opt. Express **20**, 24977 (2012).
4. A. Wojdyla, D. Bryant, W. Chao, L. Assoufid, D. Cocco, M. Idir, and K. A. Goldberg, Proc. SPIE **10760**, 1076003 (2018).
5. P. Mercère, P. Zeitoun, M. Idir, S. Le Pape, D. Douillet, X. Levecq, G. Dovillaire, S. Bucourt, K. A. Goldberg, P. P. Naulleau, and S. Rekawa, Opt. Lett. **28**, 1534 (2003).
6. P. Mercère, M. Idir, T. Moreno, G. Cauchon, G. Dovillaire, X. Levecq, L. Couvet, S. Bucourt, and P. Zeitoun, Opt. Lett. **31**, 199 (2006).
7. M. Idir, P. Mercere, M. H. Modi, G. Dovillaire, X. Levecq, S. Bucourt, L. Escolano, and P. Sauvageot, Nucl. Instrum. Methods Phys. Res. A **616**, 162 (2010).
8. B. Keitel, E. Plönjes, S. Kreis, M. Kuhlmann, K. Tiedtke, T. Mey, B. Schäfer, and K. Mann, J. Synchrotron Radiat. **23**, 43 (2016).
9. D. J. Merthe, K. A. Goldberg, V. V. Yashchuk, W. R. McKinney, R. Celestre, I. Mochi, J. MacDougall, G. Y. Morrison, S. B. Rekawa, E. Anderson, B. V. Smith, E. E. Domning, and H. Padmore, Nucl. Instrum. Methods Phys. Res. Sect. A **710**, 82 (2013).
10. L. Assoufid, X. Shi, S. Marathe, E. Benda, M. J. Wojcik, K. Lang, R. Xu, W. Liu, A. T. Macrander, and J. Z. Tischler, Rev. Sci. Instrum. **87**, 052004 (2016).
11. F. Uhlén, J. Rahomäki, D. Nilsson, F. Seiboth, C. Sanz, U. Wagner, C. Rau, C. G. Schroer, and U. Vogt, J. Synchrotron Radiat. **21**, 1105 (2014).
12. D. C. O'Shea and W. S. Rockward, Appl. Opt. **34**, 7518 (1995).
13. Y. Shiode, S. Okada, H. Takamori, H. Matsuda, and S. Fujiwara, Proc. SPIE **4691**, 1453 (2002).
14. M. Takeda, H. Ina, and S. Kobayashi, J. Opt. Soc. Am. **72**, 156 (1982).
15. J. J. Shen, SIAM Rev. **51**, 567 (2009).
16. H. Wang, C. J. Sheppard, K. Ravi, S. T. Ho, and G. Vienne, Laser Photon. Rev. **6**, 354 (2012).
17. J. W. Goodman, *Introduction to Fourier Optics*, 2nd ed. (McGraw-Hill, 1996).
18. K. A. Goldberg, D. Bryant, A. Wojdyla, M. Helmbrecht, and E. Gullikson, Opt. Lett. **45**, 4694 (2020).
19. L. Kipp, M. Skibowski, R. L. Johnson, R. Berndt, R. Adelung, S. Harm, and R. Seemann, Nature **414**, 184 (2001).
20. F. M. Huang, T. S. Kao, V. A. Fedotov, Y. Chen, and N. I. Zheludev, Nano Lett. **8**, 2469 (2008).
21. S. Le Pape, P. Zeitoun, M. Idir, P. Dhez, J. J. Rocca, and M. François, Phys. Rev. Lett. **88**, 183901 (2002).